On the Atmospheric Regulation of the Growth of Moderate to Deep Cumulonimbus in a Tropical Environment

VICKAL V. KUMAR

School of Mathematical Sciences, Monash University, and Centre for Australian Weather and Climate Research, Melbourne, Victoria, Australia*

ALAIN PROTAT

Centre for Australian Weather and Climate Research, Melbourne, Victoria, Australia*

CHRISTIAN JAKOB

School of Mathematical Sciences, and ARC Centre of Excellence for Climate System Science, Monash University, Melbourne, Victoria, Australia

PETER T. MAY

Centre for Australian Weather and Climate Research, Melbourne, Victoria, Australia*

(Manuscript received 26 July 2013, in final form 29 October 2013)

ABSTRACT

Some cumulus clouds with tops between 3 and 7 km ($Cu_{3km–7km}$) remain in this height region throughout their lifetime (congestus) while others develop into deeper clouds (cumulonimbus). This study describes two techniques to identify the congestus and cumulonimbus cloud types using data from scanning weather radar and identifies the atmospheric conditions that regulate these two modes. A two-wet-season cumulus cloud database of the Darwin C-band polarimetric radar is analyzed and the two modes are identified by examining the 0-dBZ cloud-top height (CTH) of the $Cu_{3km–7km}$ cells over a sequence of radar scans. It is found that ~26% of the classified $Cu_{3km–7km}$ population grow into cumulonimbus clouds. The cumulonimbus cells exhibit reflectivities, rain rates, and drop sizes larger than the congestus cells. The occurrence frequency of cumulonimbus cells peak in the afternoon at ~1500 local time—a few hours after the peak in congestus cells. The analysis of Darwin International Airport radiosonde profiles associated with the two types of cells shows no noticeable difference in the thermal stability rates, but a significant difference in midtropospheric (5–10 km) relative humidity. Moister conditions are found in the hours preceding the cumulonimbus cells when compared with the congestus cells. Using a moisture budget dataset derived for the Darwin region, it is shown that the existence of cumulonimbus cells, and hence deep convection, is mainly determined by the presence of the midtroposphere large-scale upward motion and not merely by the presence of congestus clouds prior to deep convection. This contradicts the thermodynamic viewpoint that the midtroposphere moistening prior to deep convection is solely due to the preceding cumulus congestus cells.

1. Introduction

Johnson et al. (1999) and Kumar et al. (2013a) provided observational evidence that convective clouds in the tropics could be grouped into three main modes: shallow cumulus with cloud-top heights (CTH, by which we mean 0-dBZ maximum top height determined with a C-band radar) near the trade inversion layer, 1–2 km above the surface; midlevel cumulus clouds with a CTH

* A partnership between the Bureau of Meteorology and the Commonwealth Scientific and Industrial Research Organisation.

Corresponding author address: Vickal V. Kumar, Centre for Australian Weather and Climate Research, Australian Bureau of Meteorology and CSIRO, GPO Box 1289, Melbourne 3001, Australia.
E-mail: v.kumar@bom.gov.au

DOI: 10.1175/JAS-D-13-0231.1

near the 0°C freezing level; and deep clouds with a CTH near the tropopause. These cumulus modes have vastly different impacts on the water and energy budgets, as well as the circulation (e.g., Tao et al. 2003; Arakawa 2004). So to improve the parameterization of convective and cloud processes in the tropics, we need to better understand the characteristics of each of these cumulus modes, atmospheric factors that determine the type of cumulus mode that will occur, and how these cumulus modes may be linked with each other (e.g., Jensen and Del Genio 2006; Jakob 2010). This study will focus on the cumulus clouds with a CTH between 3 and 7 km ($Cu_{3km–7km}$), which has been hypothesized to precondition the atmosphere for deep convection by moistening it (e.g., Sherwood and Wahrlich 1999; Derbyshire et al. 2004; Mapes et al. 2006; Holloway and Neelin 2009; Nuijens et al. 2009; Powell and Houze 2013). A separate viewpoint is that the tropospheric moistening preceding deep convection is caused by large-scale dynamics (e.g., Hohenegger and Stevens 2013; Kumar et al. 2013a). In short, the fundamental question we want to address is as follows: What causes some $Cu_{3km–7km}$ cells to stay shallow throughout their lifetime, and promotes others to grow into deep convective cells?

In this study, the observed $Cu_{3km–7km}$ cells are separated into two modes: those that cease their growth in the lower stable layer near the freezing level, referred to here as congestus (Cg) cells, and those that continue to ascend to greater altitudes to become deep convective cells at a later time, referred to here as cumulonimbus (Cb) cells. This was achieved by examining the CTH of the $Cu_{3km–7km}$ cells in a sequence of the Darwin C-band polarimetric (CPOL; Keenan et al. 1998) radar scans. We hypothesize that combining the Cg and Cb modes into the single $Cu_{3km–7km}$ category could be a reason for the limited success in understanding the possible connection between the congestus cells and deep convection. Luo et al. (2009) separated the Cg (which they referred to as ''terminal'') and Cb (referred to as ''transient'') modes using estimates of the convective buoyancy of clouds from satellite observations and Numerical Weather Prediction (NWP) analyses and found that approximately 30%–40% of the cells are Cb while the rest are Cg. However, Casey et al. (2012) noted that the method proposed by Luo et al. (2009) may be missing up to 70% of the cells compared to the criteria of cloud-top heights lying between 3 and 9 km, where there is continuous radar echo from the near ground to the cloud top (Jensen and Del Genio 2006). The Luo method detects fewer cells compared to cells detected using cloud radar (e.g., Jensen and Del Genio 2006; Casey et al. 2012) because Luo's method was applied to convective cells only. The current study also focuses on convective cells and uses new height boundaries, as proposed in Kumar et al. (2013a), to identify the various cumulus modes in the tropics. Based on an objective analysis of the behavior of radar reflectivity as a function of CTH in the Darwin region, they found a major transition of the microphysical behavior of cells once they reached a CTH of 7 km. Thus, a 7-km height threshold is used here to separate shallow cells (aka $Cu_{3km–7km}$) from deep convection.

A major motivation of this paper is not only to separate the $Cu_{3km–7km}$ cells' population into Cg and Cb modes, but also to identify the atmospheric processes that regulate the occurrence of these nongrowing and growing cumulus clouds. Several studies (e.g., Lin and Johnson 1996; Kemball-Cook and Weare 2001; Redelsperger et al. 2002; Derbyshire et al. 2004; Kikuchi and Takayabu 2004; Takemi et al. 2004; Jensen and Del Genio 2006; Nuijens et al. 2009) have noted that presence of dry air at midtroposphere can effectively limit the vertical extent of convection. Thus, if there is sufficient moistening preceding a $Cu_{3km–7km}$ cell, then it increases the likelihood for it to develop into a deep Cb tower. Early studies hypothesized that the source of the midtropospheric moistening is due to congestus cells (e.g., Sherwood and Wahrlich 1999; Mapes et al. 2006; Holloway and Neelin 2009). However, a recent study has shown that the congestus cells alone would require too long a time to produce significant moistening of the midtroposphere, which would seem to rule out the potential role of the $Cu_{3km–7km}$ moistening as a dominant process for the transition to deep convection (e.g., Hohenegger and Stevens 2013). Their findings suggested that dynamical processes, potentially related to the heating from the $Cu_{3km–7km}$ cells, are likely an important ingredient in promoting the transition to deep convection. Another possible mechanism that has been found to promote the transition from shallow cumulus to deep convection over midlatitude continental surface types is greater low-level humidity, stronger large-scale updrafts in the midtroposphere, and boundary layer inhomogeneity (e.g., Zhang and Klein 2010).

This paper is organized along two major sections. The first section outlines and evaluates two new approaches to identify the Cg and Cb cells using CTH statistics from the scanning mode of the Darwin CPOL radar observations. The difference in microphysical rainfall properties of the Cg and Cb modes is also fully characterized. The second section highlights the difference in atmospheric conditions preceding the Cg and Cb modes using both observational and derived datasets.

2. Distinguishing congestus and cumulonimbus cells in radar data

This study uses a two-wet-season dataset (October 2005–April 2006 and October 2006–April 2007) of convective

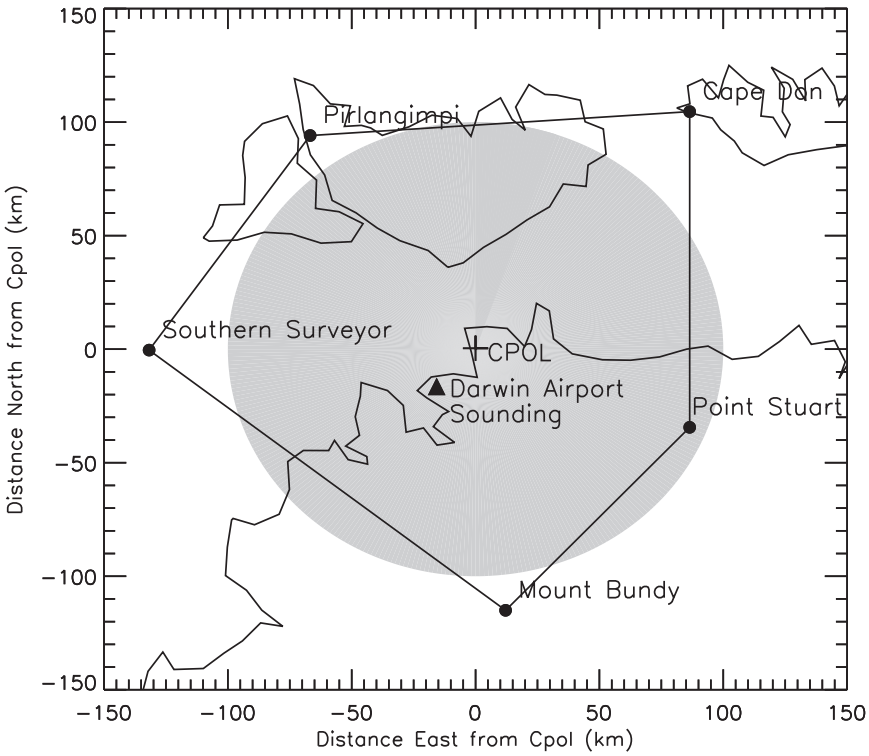

FIG. 1. The shaded gray circular region is the Darwin CPOL sampling domain. It is 100 km in radius from the radar location. The location of the operational Darwin airport radiosonde station and radiosonde stations that only operated during the TWP-ICE period are represented by a black triangle and black circles, respectively. The enclosed pentagon represents the domain for the large-scale dataset used in this study (see text for more details).

cells occurring within a radius of 100 km from the Darwin CPOL radar (12.25°S, 131.04°E; see Fig. 1). A convective cell is defined as consisting of one or more adjoining convective pixels (2.5 km × 2.5 km) using the 2.5-km radar constant altitude plan position indicators (CAPPI) data. The convective pixels are identified using the ''Steiner'' convective–stratiform classification algorithm (Steiner et al. 1995). For each convective cell, the maximum height reached by the 0-dBZ echoes above the cell is computed using reflectivity profiles to provide an estimate of the CTH. Note there must be continuous reflectivity fields in the vertical direction from the base of the cell at 2.5-km CAPPI level to the CTH (also see Kumar et al. 2013a,b). In most cases, the true cloud-top height will extend higher than the 0-dBZ CTH from a C-band radar. The difference between the C-band 0-dBZ top height and *CloudSat* CTH has been found to often be within 1 km (Casey et al. 2012). Similarly, Kumar et al. (2013a) noticed good matches between 0-dBZ cloud tops from the C-band and near −20-dBZ cloud tops from a millimeter-wavelength cloud radar (MMCR; Moran et al. 1998). Having retrieved one CTH per cell, we also calculate a single mean reflectivity, rain rate, drop size diameter (D_0) and number concentration of small hydrometers (N_W) for each convective cell. These mean values were calculated using the radar pixels at the 2.5-km level that are bounded by the horizontal cross-sectional area of the cell.

Descriptions of the algorithm used to retrieve drop size distributions (DSD) parameters and rain rates from the CPOL observations are given in Bringi et al. (2009). The algorithm assumes a normalized gamma DSD form (Testud et al. 2001) described by the median drop size diameter (D_0, mm) and the ''generalized'' intercept parameter (N_w). For simplicity, N_w can be thought as the number concentration of small hydrometers and has units of meters cubed per millimeter (the number concentration of hydrometeors per unit diameter). The parameter N_w is the same as the intercept parameter of an exponential DSD with the same D_0 and liquid water content as the gamma DSD. This algorithm uses a multiparameter approach to take advantage of the complementary information contained in the polarized backscattered signals. First, D_0 is retrieved from the differential reflectivity using polynomial fits [e.g., $D_0 = f(Z_{\rm dr})$], then N_w is estimated using a power law of

the form $Z_h/N_w = c(D_0)^d$, and finally the rain rate is estimated using either a function of the form $R = f(K_{dp})$, $R = f(Z_h, Z_{dr})$, or $R = f(Z_h)$, depending on various thresholds and a decision tree (Bringi et al. 2009).

The Darwin CPOL radar operates at wavelength of 5.3 cm, with a minimum detectable reflectivity of −1.25 dBZ up to a radar range of 100 km. At this wavelength and radial distance, the radar will not be able to detect clouds made of drops of sizes less than 0.5 mm. Such clouds, which normally are classified as nonprecipitating clouds, are typically studied using millimeter wavelength cloud radars. Kumar et al. (2013a) have carried out a comparison between the cloud occurrence frequency detected by the Darwin CPOL and the Darwin MMCR radars. They found that the CPOL radar has a detection efficiency of 30% compared to MMCR for shallow cumulus clouds (CTH < 3 km; e.g., Zhang and Klein 2010) increasing to a 64% detection efficiency when the CTH is between 3 and 7 km (also known as $Cu_{3km–7km}$). Since CPOL misses most of the shallow cumulus cells, statistics associated with shallow cumulus category were removed from the subsequent analysis.

Over the two-wet-season study interval, CPOL detected a total of 207 871 cells with a CTH between 3 and 7 km—the $Cu_{3km–7km}$ cells. A 7-km CTH threshold is used instead of the often-used 9-km cutoff (e.g., Jensen and Del Genio 2006) because convective cell reflectivities and the DSD parameters exhibit clear microphysical differences when the CTH of the cells are less than 7 km compared to those that extended beyond 7 km (e.g., Takemi et al. 2004; Kumar et al. 2013a). Having identified the $Cu_{3km–7km}$ cells, the next task is to distinguish cells that will continue to rise above 7 km during their lifetime (Cb cells) from those that will not (Cg cells). Here, we employ two different methods.

Method 1 is a ''nearest neighbor'' approach. It employs the same logic as that used in the automated Thunderstorm Identification Tracking Analysis and Nowcasting (TITAN) radar analysis tool (Dixon and Wiener 1993). Note the current TITAN settings of a minimum volume requirement of 30 km^3 and the reflectivity threshold of 35 dBZ are fine tuned to identify deep convection. The tool has not been optimized to detect the less intense $Cu_{3km–7km}$ cells, and so cannot be used directly for our purpose. We therefore only use the TITAN cell speed and direction products to assist in establishing the potential search area to find the nearest neighbor for the test $Cu_{3km–7km}$ cells in the subsequent scan. The TITAN tool tracks the cloud cells in space at discrete times (every 10 min in this case) and so the velocity vectors of cloud cells through their lifetime were determined from relative motion of the cells. During times when the TITAN tool does not detect any cell track, the cell speed and direction is determined through an interpolation process of neighboring TITAN cell statistics.

The search area used in method 1 has a rectangular layout as highlighted in Fig. 2. This rectangle is positioned in such a way that the enclosed test $Cu_{3km–7km}$ cell is 5 km from its nearest two edges. The overall length of the north–south edge of the search rectangle is equal to twice the product of the meridional component of the 10-min median TITAN cell speed and the time to next scan (10 min) plus the offset of 5 km. The length of the east–west edge is calculated in the same way except using the zonal component of the TITAN cell speed. Note that some of the choices to establish the search area are somewhat arbitrary and have been selected as a compromise between having a sensible search area (not too large) while keeping a good chance of tracking the cell over its entire lifetime. Sensitivity studies changing those settings produced similar results to the ones used here.

Figure 2 shows the three different scenarios that could occur in the search area. Cell A is flagged as Cg cell since its subsequent stage has lower CTH compared to the previous scan. Cell B highlights the scenario where its nearest neighbor has a higher CTH compared to previous scan. In such situations, the $Cu_{3km–7km}$ cell is tracked over several subsequent scans until its CTH has been found to have either exceeded 7 km (thus flagged as Cb cell) or its CTH never exceeded 7 km throughout its lifetime (flagged as Cg cell). Cell C had no neighbor but is still flagged as Cg cell because there is a possibility that the test cell decayed by the time the subsequent radar scan was completed.

Method 2 is based on a probabilistic approach. The search area is defined in the same way as in method 1, except we examine up to six subsequent radar scans before making a decision. Here a cell is flagged as Cg cell if over the next six subsequent radar scans, at least 80% of the convective cells have CTH < 9 km; that is, the test $Cu_{3km–7km}$ cell has a high probability of never growing into a deep convective cell. Similarly, a cell is flagged as Cb when at least 50% of the convective cells over the next three radar scans are deep convective cells (CTH > 9 km); that is, the test $Cu_{3km–7km}$ has a high probability of growing further. We deliberately used a higher probability threshold of 80% for Cg cells and a moderate one of 50% for Cb cells because at any given time one would expect that there will be more Cg cells than deep convective ones. Other settings, such as height thresholds of 7–9 km, CTH occurrence ratios of 20%–90%, as well as different area multiplication factors (2–6 times) and lead times (20–120 min), have been tested and the results are similar.

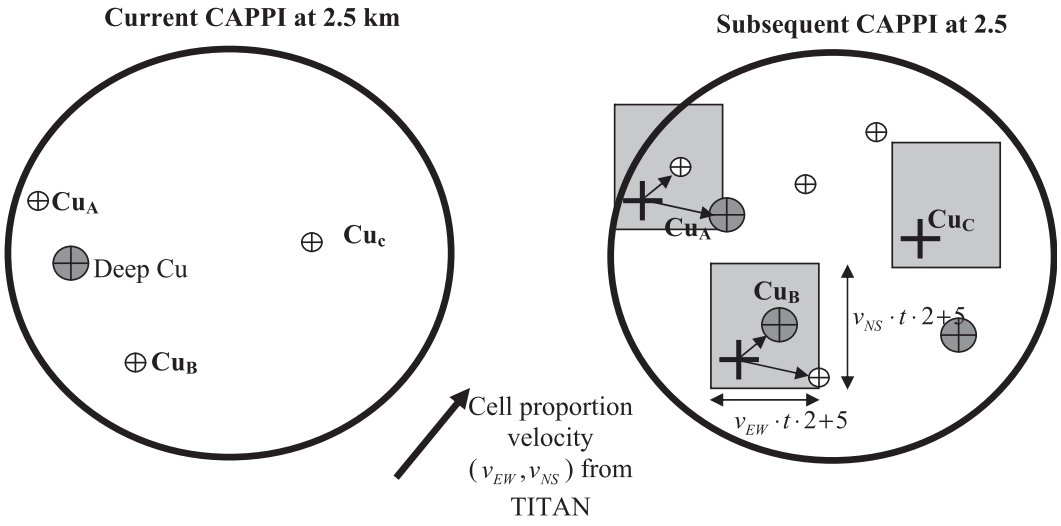

FIG. 2. Schematics for identification of congestus (Cg) and cumulonimbus (Cb) cells using the nearest neighbor approach (method 1). (left) Current radar CAPPI snapshot at 2.5-km level with three $Cu_{3km–7km}$ cells (Cu_A, Cu_B, Cu_C, smaller circles with crosses) and one deep cell (large circle with cross and gray filling). (right) Subsequent CAPPI snapshot after a scanning time of 10 min; the gray shaded rectangle is the search area (see text) and the large dark crosses represent the initial location of the cumulus cells. The nearest neighbor of Cu_A has a lower CTH than that of Cu_A; thus, it is an example of a Cg cell. The nearest neighbor of Cu_B has a higher CTH and represents the scenario where Cu_B can be classified as Cg or Cb depending on maximum CTH reached by this cell as it is tracked further through its entire lifetime. The cell Cu_C has no appropriate neighbor and is considered a Cg cell.

Figure 3 shows the overall results for all $Cu_{3km–7km}$ cells described above. The shaded gray region is the probability distribution function (PDF) for reflectivity at the 2.5-km CAPPI level associated with all the 207 871 $Cu_{3km–7km}$ cells in the sample. The solid and dashed curves represent the PDFs associated with Cg and Cb cells, respectively. The black and red curves are using data points detected by the two different methods discussed above. The bars plotted along the PDF curve in this figure represent the scatter in reflectivity PDFs arising from the sensitivity to parameter settings in the search algorithms. Note the current choices for each method are determined through a trial and error approach such that the difference between the Cg and Cb cells are most clear.

Both methods show that the Cg cells (solid lines) have a higher probability of having low reflectivity values compared to the overall distribution (shaded gray region). Similarly, the Cb cells (dashed lines) have a higher probability of having larger reflectivities. The modal reflectivity bin for the Cg cells is 35 dBZ with both methods and that of Cb cells is around 40 dBZ, with a slightly broader distribution in method 1.

Out of the more than 200 000 $Cu_{3km–7km}$ cells detected over the two wet seasons, method 1 flagged 82% as Cg cells and 18% as Cb cells. Fifty-one percent of the Cg cells had no subsequent nearest neighbor, indicating that they were very short lived. Note that because of the radar wavelength, we only detect the precipitating stage of the cells. Removing these short-lived cells from the analysis leads to a drop in reflectivity probabilities, particularly in the lower reflectivity bins (<25 dBZ; Fig. 3). Method 2 identifies 51% of the $Cu_{3km–7km}$ population

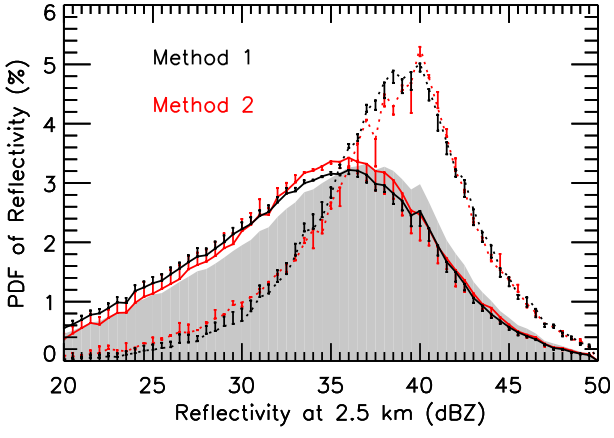

FIG. 3. Distribution of reflectivity using a bin size of 1 dBZ for the Cg (solid line) and Cb (dotted line) cells. The reflectivity is taken at the 2.5-km CAPPI level, where one mean reflectivity value is obtained per convective cell. The gray shaded region represents the PDF obtained using all $Cu_{3km–7km}$ cells (top height < 7 km). The black and red curves are the PDF values obtained using two different methods of classifying the Cg and Cb cells. The bars plotted along each curve represent the sensitivity to parameter settings in each method (see text for more details).

as Cg and 18% as Cb. The remaining 31% of the $Cu_{3km–7km}$ cells are not classified because the ratio of the number of $Cu_{3km–7km}$ to deep convective cells is within the uncertain range of 50%–80%, showing a limitation of this methodology.

The excellent agreement in the frequency of occurrence of Cb cells indicates that both methods are robust and not unduly sensitive to the thresholds used in each method. However, the Cg cell occurrence counts do show a significant discrepancy. The extra 30% Cg cells identified using method 1 are predominantly of the short-lived type (cell C in Fig. 2). Visual inspection of radar loops around several of the Cg cells that were classified by method 1 but not with method 2 confirms that these cells often occur in a single image only, hence indicating a lifetime of 10 min or less. To avoid biasing our results to those short-lived cells, we will only use data from the more conservative method 2 for the rest of our discussion. The 18:51 ratio between Cb and Cg found using method 2—that is, for every Cb cell there will be 2.8 Cg cells—is comparable with the 30:70 ratio (1 Cb is to 2.3 Cg cells) found in Luo et al. (2009). This provides a good test since the cell identification method used in this paper and the method used in Luo et al. (2009) are both looking at only genuine convective cells.

3. The basic properties of the congestus and cumulonimbus cells

The rainfall and cloud properties over the Darwin region have been shown to be strongly regulated by the large-scale environment (May et al. 2012; Kumar et al. 2013b; Penide et al. 2013). Pope et al. (2009) identified an effective way to divide the synoptic conditions in Darwin into five physically meaningful states. We first use this synoptic classification to study the effect of these large-scale states on the Cg:Cb ratio. The ratios of Cb to Cg cells were found to be largely insensitive to the large-scale regimes, with ratios of 25:75 during all five large-scale regimes. Overall, the deep westerly (DW) regime, which is associated with active monsoon conditions, contributed the most to the overall two season Cg and Cb cell totals. The second highest contribution was from the moist easterly (ME) regime. This regime is associated with the typical monsoon break conditions, and was the most frequent (157 out of 293 days) of all the regimes. The combined contribution from the remaining three regimes to the $Cu_{3km–7km}$ totals was less than 15%. Hence, these three regimes will not be discussed further.

Figure 4 shows the normalized diurnal variations of the relative occurrence of the Cg (solid lines) and Cb (dashed lines) modes for all cases and separately for the DW (crosses, 59 days) and ME (diamonds, 157 days) regimes. The overall pattern of the $Cu_{3km–7km}$ population shows a late morning to midday peak in all regimes (not shown). In the ME regime, this peak is contributed by a relative increase in Cg cells around midday, followed by relative increase in Cb cells in the afternoon and evening hours. The afternoon peak of Cb cells is indicative of the well-known often sea-breeze-driven diurnal cycle of deep convection in Darwin during monsoon buildup and break conditions. In contrast, the diurnal variability in the DW regime is weak. As the DW regime represents monsoon conditions, this is likely the result of the presence of continuous cloud cover reducing daytime heating and thus suppressing sea-breeze-driven convection (e.g., May et al. 2012; Kumar et al. 2013b).

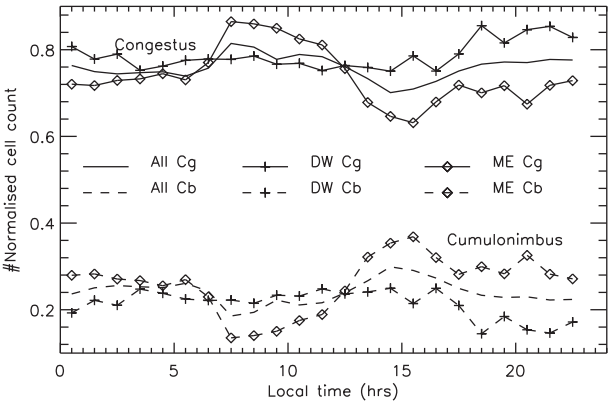

FIG. 4. Diurnal variations of the relative Cg (solid line) and Cb (dashed line) cell counts over the two-wet-season study interval for the DW (crosses) and ME (diamonds) regimes. A bin size of 1 h in local time is used here. In each local time bin, the occurrence frequency of the Cg and Cb cell are normalized such that their sum is always 1.

We now investigate some of the rainfall properties of the Cg and Cb modes making use of the polarimetric capabilities of the CPOL radar (e.g., Zrnić and Ryzhkov 1999; Bringi et al. 2009). Figure 5 shows the distribution of the reflectivity, rain rate, median raindrop volume diameter (D_0), and the number concentration of small hydrometers (N_w) as function of CTH using box–whisker plots. The CTH varies from 3 to 7 km in steps of 0.5 km. Recall that each $Cu_{3km–7km}$ cell is assigned a single mean rainfall parameter, obtained using radar data from the 2.5-km CAPPI level bounded by the horizontal cross-section area of the cell. In Fig. 5, the boxes represent the 25th and 75th percentiles with the thick gray box indicating all $Cu_{3km–7km}$ cells, the thin black box the Cg cells, and the thin striped box the Cb cells. The curves represent the median value for each $Cu_{3km–7km}$ cloud-top group, and the whiskers are the 5th and 95th percentiles

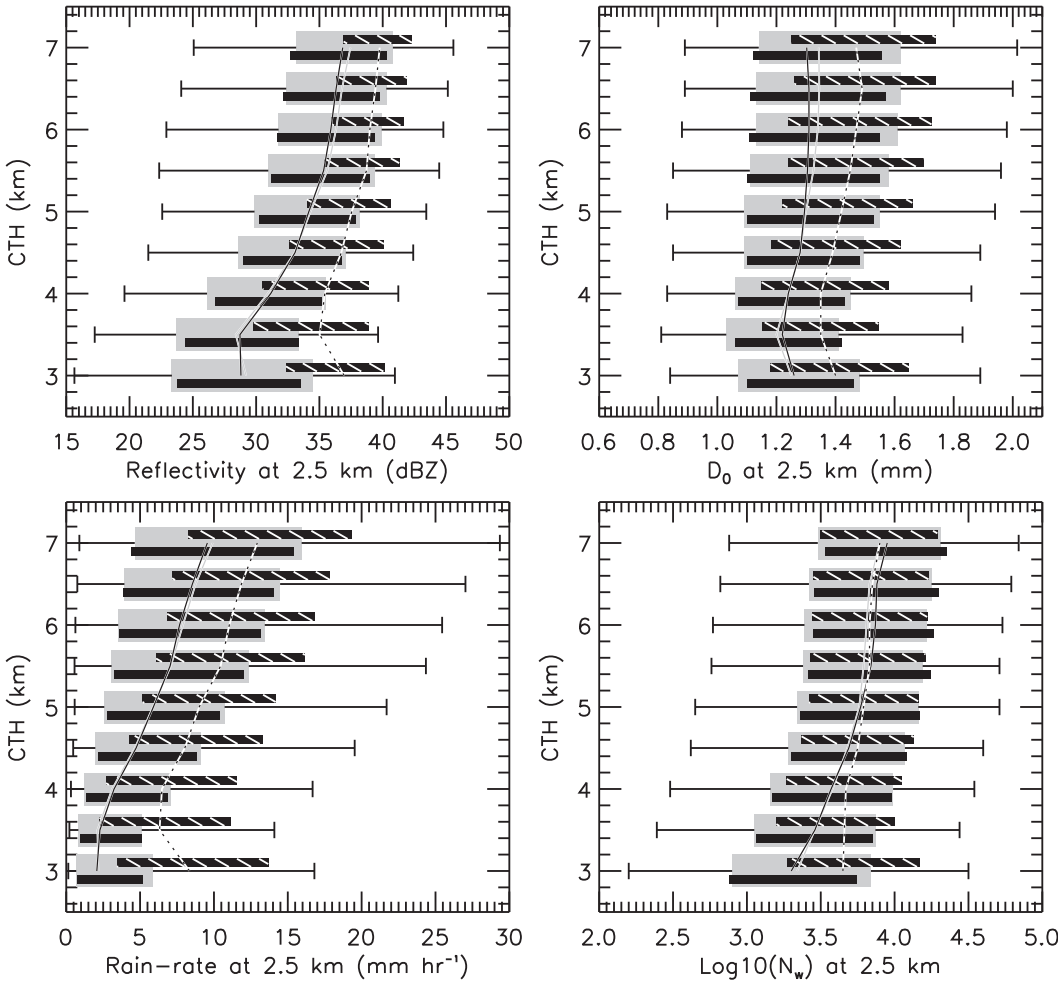

FIG. 5. Box–whisker plots in 0.5 km steps of CTH of (top) (left) reflectivity and (right) median drop size diameter (D_0); and (bottom) (left) rain rate and (right) number concentration of small hydrometers [log10(N_w)]. As in Fig. 3, a single mean value is obtained per cloud cell. The thick gray box (25th and 75th percentiles) with whiskers (5th and 95th percentiles) represents results using all the data. The thin black rectangle shows results for the Cg cells only. Similarly, the striped rectangles show the results for the Cb cells. The curves (solid gray for all cells; solid black for Cg; dashed for Cb) are the median values for each CTH level.

associated with all the $Cu_{3km–7km}$ cells. The whiskers for the Cg and Cb cells are omitted.

For the $Cu_{3km–7km}$ populations as the whole, the median reflectivity at 2.5 km shifts toward higher values (top panel) as the CTH increases while the distribution gets narrower. A positive correlation between near ground cell reflectivity and maximum height reached by cloud cell is typical since larger reflectivities generally correspond to stronger growth momentum (e.g., Zipser and Lutz 1994). In accordance with these results, the cell rain rate increases with CTH. The median raindrop size D_0 is almost invariant with CTH showing a very small increase as the cloud depth increases. The concentration of small hydrometeors increases by almost an order of magnitude as the cells deepen.

The behavior of the cloud properties shows some distinct differences between the Cg and Cb classes. Overall, for any given CTH the Cg cells have smaller mean reflectivity, lower rain rate, and smaller drop size at 2.5-km height than the Cb cells with the same CTH. The median reflectivity, rain rate, and drop size in the Cb cells exceed that of the Cg cells by 5 dBZ, 3 mm h^{-1}, and 0.18 mm, respectively. However, the N_w, parameter exhibited no obvious difference between the Cg and Cb cells, except in the shallowest $Cu_{3km–7km}$ cells with CTH below 4 km.

Despite the large mean (or median) differences between the Cg and Cb modes, there is a large overlap of the distributions of the rainfall properties. In other words, the radar parameters here cannot be used easily

to predict how an emerging $Cu_{3km–7km}$ cell will develop and in which class it will ultimately fall. However, it appears that the 25th percentile reflectivity level in the Cb cells is often very close to the overall median of all the $Cu_{3km–7km}$ cells. The largest separation between the Cg and Cb distribution occur when the CTH is small. We also investigated potential differences in the vertical profile of reflectivity lapse rate (e.g., Zipser and Lutz 1994) for the Cg and Cb modes (not shown). As before, the differences in this parameter did not serve as a confident proxy for separating the Cg and Cb cells. We hypothesize that the updraft speeds in the convective core, which can be obtained using Doppler radar techniques, may be a better criterion to distinguish between the Cg and Cb cells. Presumably, the Cb cells are likely to have a stronger updraft speed since they grow into deep convective clouds at a later time.

4. Atmospheric factors affecting the growth of convective cloud cells

The goal of this section is to identify key atmospheric processes that may determine the growth or suppression of $Cu_{3km–7km}$ cells and hence regulate if clouds will fall into the Cg or Cb classes defined above. Several hypotheses to explain the shallow to deep cloud transition in tropical convection have been put forward in the recent literature:

1) Moistening of the midtroposphere by $Cu_{3km–7km}$ cells precedes the onset of deep convection (e.g., Sherwood and Wahrlich 1999; Mapes et al. 2006; Holloway and Neelin 2009).
2) The moistening of the midtroposphere is caused by large-scale dynamical processes leading to ascent. The ascent is potentially related to heating from $Cu_{3km–7km}$ cells, causing moisture convergence (e.g., Hohenegger and Stevens 2013; Kumar et al. 2013a).
3) Increased boundary layer inhomogeneity in the thermodynamic and wind fields causes the rising cloud parcels to have more momentum, which increases the probability of clouds reaching the level of free convection and develop into deep convection (e.g., Zhang and Klein 2010).

Hypothesis 3 focuses largely on the transition from shallow, nonprecipitating convection to deep convection. Therefore, it cannot be reliably tested in this study, since we cannot reliably detect fair-weather shallow cumulus clouds. Both the Cg and Cb modes have already grown past the trade inversion layer. We will therefore focus on evaluating hypotheses 1 and 2 in what follows.

Hypothesis 1 and 2 are based on the premise that moistening of the midtroposphere occurring prior to deep convection is crucial for the formation of deep convection—often referred to as preconditioning. So we begin the analysis by testing this preconditioning requirement using the relative humidity and temperature measurements from radiosonde observations at Darwin airport (see Fig. 1 for the sounding location). The radiosondes operated typically at 6-h intervals. Since the Cg and Cb modes as well as the subsequent deeper mode rarely occur in complete isolation, special care has to be taken in establishing the link between the variations in atmospheric conditions and the growth of the two $Cu_{3km–7km}$ modes.

To do so, two procedures are applied here: The first step identifies times where one of the $Cu_{3km–7km}$ modes is dominant over the other. To achieve this, the ratio of the Cb cell count to the total (Cb + Cg) is calculated in bins of 6 h. A 6-h data block is flagged as dominated by the Cg mode if the ratio of the Cb to the total is below 12%—the lower tercile of the 6-hourly Cb to total ratio distribution. Similarly, if the 6-hourly ratio exceeded 38%, the upper tercile of the Cb to total ratio distribution, the data block is flagged as dominated by the Cb mode. Only Cg cells (Cb cells) that formed in the 6-hourly Cg dominated data blocks (Cb dominated data blocks) are kept for further analysis. This filtering process leaves ~42 000 Cg cells (40% of the original Cg population) and ~16 600 Cb cells (44% of the Cb population).

The second step of our analysis procedure aims to filter out atmospheric environments that may have already been modified by deep convection. Because of the high time resolution of the radar observations, the timing of the radiosonde ascents relative to the occurrence of the $Cu_{3km–7km}$ modes is random. It can be as little as 10 min and as much as 6 h before or after the cloud observations. As we wish to focus on the effects of the environment on the $Cu_{3km–7km}$ clouds, rather than the other way around, only radiosonde data with an occurrence time between 0 and 6 h prior to the detection time of the Cg and Cb cells are included in the analysis.

Figure 6 shows the joint frequency distributions of relative humidity (top panels) and temperature lapse rate (bottom panels) as a function of height for the Cg (left column) and Cb (right column) cells derived from radiosonde ascents 0–6 h before the radar image as described above. These two atmospheric parameters were chosen as they have been previously deemed to play a role in limiting the vertical extent of cumulus clouds (e.g., Derbyshire et al. 2004; Takemi et al. 2004). The difference between the distributions of relative humidity (Fig. 6, top panels), in particular above the altitude of 5.0 km, in the Cg and Cb modes is quite remarkable. The midtroposphere is clearly much drier in periods with

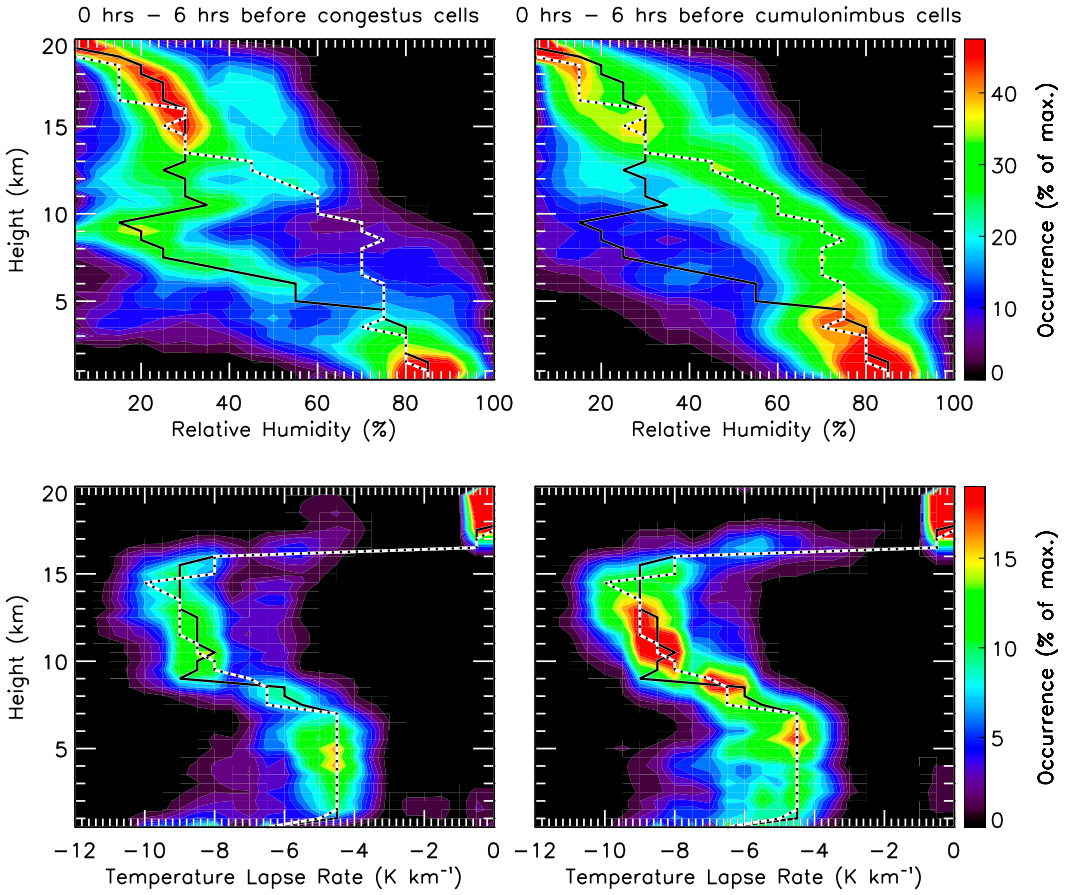

FIG. 6. (top) The vertical profile of relative humidity using of 5% size bins and (bottom) temperature lapse rate using 0.5 K km^{-1} size bins for (left) Cg and (right) Cb cells. The solid and dashed lines represent the values for the Cg and Cb modes, respectively; these have been overlaid for easier comparison.

predominantly Cg cells than in those with large numbers of Cb cells. The most notable feature is the abrupt drop in relative humidity from a modal value of 72% at 5 km to only 30% at 7.0 km associated with the Cg cells. The temperature lapse rate distributions associated with the two $Cu_{3km–7km}$ modes are found to be very similar (Fig. 6, bottom panels), except that the temperature lapse rates distributions are slightly broader for the Cb cells. The results shown in Fig. 6 are consistent with the viewpoint that entrainment of dry ambient air into the cells can play a key role in limiting the vertical extent of convection (e.g., Redelsperger et al. 2002; Derbyshire et al. 2004; Takemi et al. 2004; Jensen and Del Genio 2006). A key question remaining is to identify the source of the moistening preceding the Cb cells or drying preceding the Cg cells.

5. Sources of midtroposphere moistening preceding the development of cumulonimbus cells

In this section we aim to investigate what processes are involved in moistening the midtroposphere in the hours leading up to the onset of the predominantly Cb cell population. It is worth recalling that the two main processes are a moistening by $Cu_{3km–7km}$ cells (hypothesis 1) and moistening that involves large-scale dynamical processes (hypothesis 2).

Hypothesis 1 is tested by performing a composite analysis of relative humidity and occurrence frequency of two $Cu_{3km–7km}$ modes for the 6 h preceding the onset of the Cg and Cb cells. The results are shown in Fig. 7. For this analysis, the radiosonde data used are the same as those employed in Fig. 6, except that now we show the temporal evolution of relative humidity. The radiosonde data are divided into 1-h bins of time and 0.5-km bins of height, and the median is calculated separately for each bin and displayed in Fig. 7. The short vertical lines (which appear nearly continuous) above the humidity panels represent the actual timestamps of the radiosonde data used in this analysis. It is clear from this illustration that the radiosonde data is drawn from nearly all times leading up to the cell identification, providing confidence that the results are robust on an hourly scale

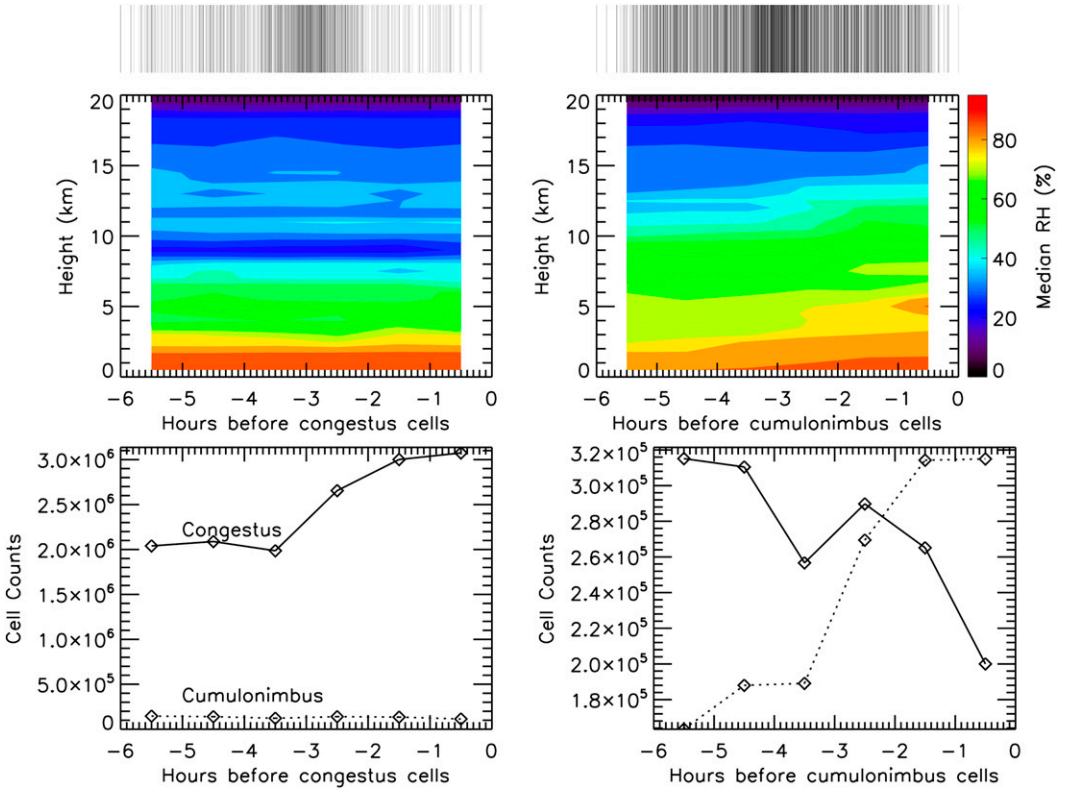

FIG. 7. Composite evolution of the (top) 6-hourly relative humidity and (bottom) radar cell occurrence frequency for the 6 h preceding the onset time of (left) terminal and (right) transient cells. The vertical black lines above the relative humidity tendency panels indicate the actual radiosonde times used in the composite analysis.

despite using the 6-hourly radiosonde data. The bottom panels show the composite count of the all Cg (solid curve) and Cb (dashed curve) cells.

The top panels of Fig. 7 show that conditions in the time leading up to Cg cells are distinctly different to those for Cb cells. In the case of Cg cells, the atmosphere above the boundary layer (but not the boundary layer itself) is significantly drier and this structure does not change in the 6 h leading up to the Cg cell event. The Cb cell cases are generally characterized by moister conditions even 6 h before the event, indicating an important difference in the meteorological background state associated with the two $Cu_{3km-7km}$ modes. Consistent with both hypotheses of preconditioning, the relative humidity, especially in the midtroposphere, increases before the onset of Cb cell events. The increase appears particularly rapid about 3 h before the event.

The bottom panels of Fig. 7 show that there is a large population of Cg cells leading up to both Cg and Cb cell events. Within 3 h preceding the Cg events, the incidence of Cg cells increases without any significant change in the vertical relative humidity distribution. This is interesting as it indicates that the increased number of Cg cells is not able to moisten the midtroposphere by itself, implying either strong compensating drying processes or a lack of efficiency in the moistening from $Cu_{3km-7km}$ cells alone. Similar to the findings in Fig. 4, it is evident that Cb cell events are preceded by a high occurrence of Cg cells a few hours before the transition to deeper cells. Thus, on face value the Cg cells appear to be a key ingredient to precondition the troposphere for the subsequent development of Cb cells, which eventually leads to the development of deep convection. However, a significant population of Cg cells also exists in the hours leading up to the occurrence of mostly Cg events. This clearly indicates that other processes must also be important in regulating the formation of Cg and Cb cells (hypothesis 2). This is explored next.

The investigation of the relative role of large- and small-scale processes in determining cloud depth requires reliable estimates of the large-scale state concurrent with the radar observations. Such datasets are typically derived from radiosonde arrays deployed during field campaigns or are simply derived from operational NWP analysis or reanalyses performed with

NWP systems. Using data from the Tropical Warm Pool International Cloud Experiment (TWP-ICE; May et al. 2008), Davies et al. (2013) have demonstrated that the use of NWP analysis at high time frequency is not justified owing to the poor quality of the divergent wind, and hence vertical motion field, in these analyses. However, they also showed that long records of reliable estimates of the large-scale budgets around Darwin can be derived by applying the variational budget analysis technique of Zhang and Lin (1997) using NWP analysis data as ''pseudo radiosondes'' and observations at the surface and top of the atmosphere, as suggested by Xie et al. (2004). The resulting large-scale dataset used here, which is often referred to as the forcing analysis, includes vertical profiles of heat and moisture budgets as well as thermodynamic and dynamic variables at 40-hPa vertical and 6-h temporal resolutions. The domain represented by this dataset is shown by the pentagon shape in Fig. 1 and is comparable to the CPOL domain used here (shaded gray circle).

The large-scale forcing dataset contains several parameters relevant to convection. Table 1 provides an overview of some of those parameters showing the 95% confidence intervals of their mean.[1] Note that the forcing dataset has been processed in the same manner as the radiosonde dataset above in that only profiles from the preceding 6 h relative to cell identification as Cg and Cb dominated are used in the analysis. Results shown in Table 1 reveal that the mean convection inhibition (CIN), surface evaporation, and midtroposphere (300–600 hPa) temperature preceding the two congestus modes are similar at the 95% confidence level. Thus, these factors are unlikely a cause for congestus clouds to grow in deep convection. In contrast, both the large-scale vertical motion (omega) in the midtroposphere and thus the vertical advection of moisture, as well as the convective available potential energy (CAPE), are clearly larger in the intervals preceding Cb cell than in those ahead of Cg cells. Similarly, the low-level horizontal winds and thus potentially the horizontal advection of moisture are also significantly different between the two $Cu_{3km-7km}$ modes. One possible explanation for these differences is that the different cell modes occur in different meteorological regimes, such as the Darwin monsoon (the DW regime) and break (the ME regime) conditions, which are known to have very different thermodynamic and wind profiles (Pope et al. 2009). This is further explored next.

TABLE 1. Mean atmospheric conditions associated with the Cg and Cb cells. The data ranges represent the 95% confidence intervals about the mean (see text for details).

	Cg cells	Cb cells
Total number of cells analyzed	42 028	16 613
CAPE ($J\,kg^{-1}$)	267.3–292.3	570.9–603.3
CIN ($J\,kg^{-1}$)	22.4–25.1	23.8–25.2
Surface evaporation ($mm\,h^{-1}$)	0.38–0.40	0.34–0.35
300–600-hPa water mixing ratio ($g\,kg^{-1}$)	4.27–4.61	4.44–4.79
300–600-hPa RH (%)	60.3–62.4	63.9–65.5
300–600-hPa temp (K)	272.9–274.4	272.7–274.2
300–600-hPa omega ($hPa\,h^{-1}$)	−0.92 to −0.52	−2.82 to −2.44
600–1015-hPa HADV ($g\,kg^{-1}\,h^{-1}$)	−0.049 to −0.037	−0.021 to −0.016
600–1015-hPa horizontal advection of temperature ($K\,h^{-1}$)	0.049–0.061	0.027–0.037
600–1015-hPa westerly (u, $m\,s^{-1}$)	5.32–6.00	1.71–2.17
600–1015-hPa southerly (v, $m\,s^{-1}$)	−0.71 to −0.47	−1.40 to −1.14
600–1015-hPa wind speed ($m\,s^{-1}$)	7.41–8.13	4.89–5.42
600–1015-hPa wind shear ($m\,s^{-1}\,hPa^{-1}$)	0.024–0.030	0.030–0.032

We begin this by examining the vertical profiles of all the four terms in the large-scale moisture budget expression (Fig. 8). This expression can be defined as

$$\frac{\partial q}{\partial t} = \nu_H \cdot \nabla_H q + \omega \frac{\partial q}{\partial p} + Q2.$$

In the above, most of the notations are convectional; $\partial q/\partial t$ is the moisture tendency, which for sake of simplicity will be referred to as q tend. The q tend term arises from contributions from large-scale horizontal advection ($\nu_H \cdot \nabla_H q$ or simply HADV), vertical advection ($\omega \partial q/\partial p$ or VADV), and the residual term (Q2). The Q2 term represents the collective effects of all subdomain-scale processes (see Yanai et al. 1973). All terms are scaled to the same units of humidity change with time (i.e., $g\,kg^{-1}\,h^{-1}$).

The top panels of Fig. 8 show the mean profiles of large-scale moisture budget using all data points occurring within 6 h preceding the 42 000 Cg and 16 600 Cb cells. The middle and bottom panels separate these results into the DW and ME regimes, respectively. Note that ~50% of the 42 000 Cg cells used in these calculations occurred during the DW regime; thus, the mean behavior in the top left panel of Fig. 8 associated with all Cg cells will be strongly influenced by the DW regime.

[1] A set of 100 different mean values are generated using a randomly selected samples from the main batch of data. Then the 95% confidence interval is extracted from probability distribution function of the means (e.g., Chu and Wang 1997).

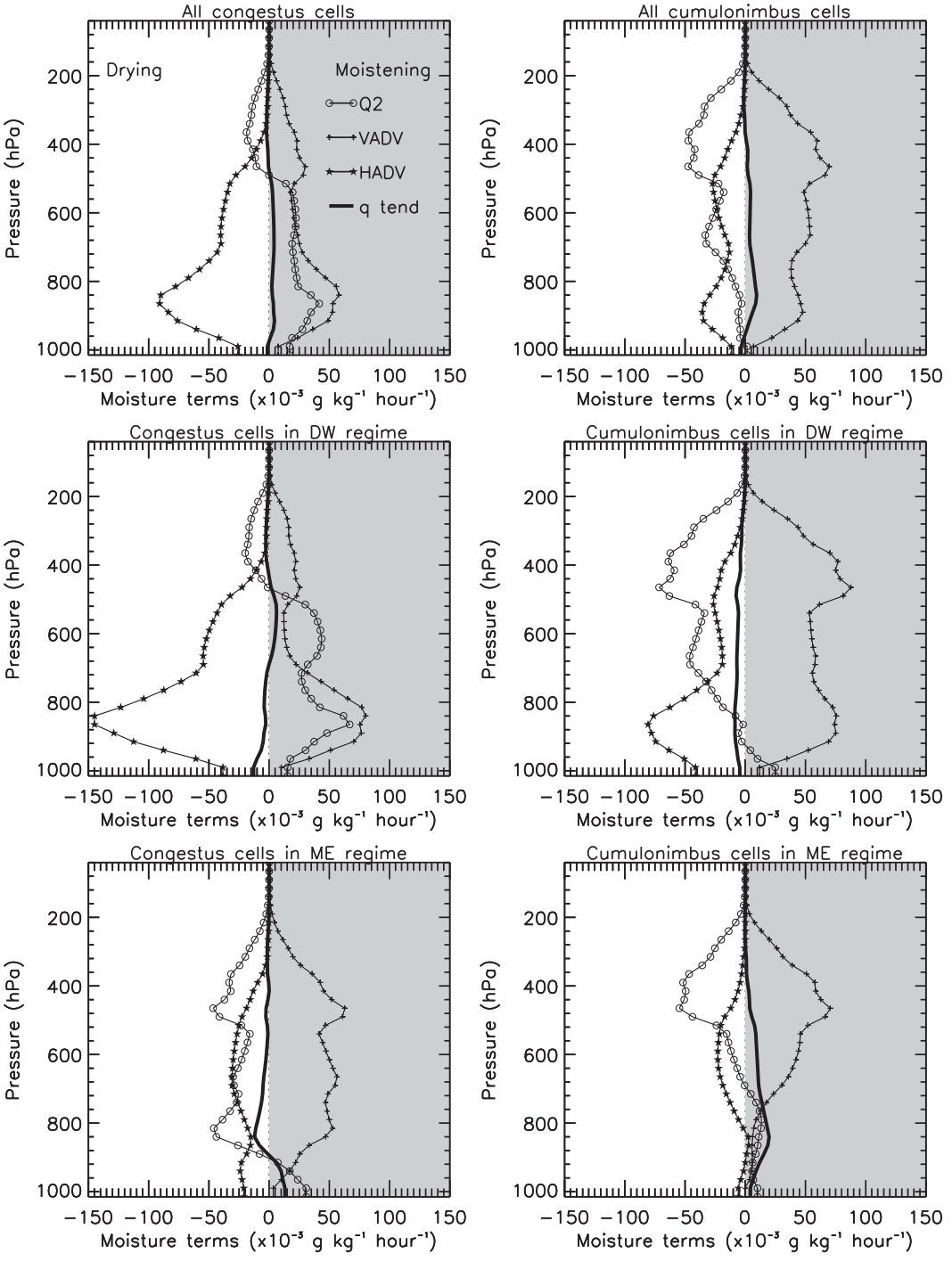

FIG. 8. Mean vertical profiles of the moisture budget terms preceding the (left) Cg and (right) Cb cells. (top) Results for all data, (middle) DW regime, and (bottom) ME regime. The shaded gray region represents moistening, while the white area indicates drying.

The Cb cells (right panels of Fig. 8) were most frequent in the ME regime (~42% of the 16 600 cells), followed by the DW regime (35% of the cells). Two features are found to be different between the Cg and Cb modes and these were reproducible regardless of the atmospheric regimes (hence can be considered genuine factors in regulating the growth of Cg and Cb cells) included:

1) The large-scale vertical advection causes moistening of the midtroposphere (300–600 hPa) preceding both cloud modes. However, this moistening is larger preceding the Cb cells than preceding the Cg cells.
2) Greater drying by large-scale horizontal advection in the low levels (600–1015 hPa) preceding the Cg cells than preceding the Cb cells.

In contrast, the Q2 and q tend terms associated with the different large-scale regimes are found to exhibit different signatures. For example, the subgrid processes (Q2) moisten the troposphere between 600 and 1000 hPa preceding the Cg cells only during the DW regime (thus also shows in overall average; Fig. 8) and not during the other conditions. This moistening by Q2 has been linked to evaporation of precipitation from stratiform clouds, which are widespread in the DW regimes (Kumar et al. 2013a,b). Thus, the responses in Q2 term and so in q tend are thought to be a result of different synoptic environments of the two regimes themselves and are less likely to explain why some $Cu_{3km–7km}$ cells grow and others remain shallow throughout their lifetime.

It is clear from the discussion above that there is a strong relationship between the growth of Cb cells into deep convection and the moistening of the midtroposphere in the hours preceding the onset of Cb cells. The moistening preceding the Cb cells appears to be linked to either one or both of the following causes: the preceding Cg cells and/or large-scale vertical advection (as the horizontal advection terms are almost always negative, so leads to drying). We now investigate the competing contributions of these two factors in increasing the moisture of the midtroposphere.

It is tempting at first glance to ascribe the midtroposphere moistening associated with the growth of Cb cells to the occurrence of Cg cells, which peaks a few hours before the Cb cells (Figs. 4 and 6). However, this is inconsistent with the findings for the Cg cell events themselves, which show Cg cells existing for long periods of time with no effect on the midtroposphere relative humidity and with few Cb and deep cells forming in the subsequent period. To study this further, we first identify peak Cg cell occurrence events, characterized by a Cg cell frequency larger than 42 cells per hour. This value corresponds to the upper tercile of all hourly Cg cell counts. A total of 275 such events were identified from our two wet-season database.

The top panel of Fig. 9 shows the results of a composite analysis of the mean Cg cell (solid) and Cb cell (dashed) frequencies around these events, separated into three bins of the midtroposphere large-scale vertical advection of moisture. The vertical advection values are taken at the 500-hPa level, $VADV_{500}$, and at the nearest time to the onset of events. There are 75 events with $VADV_{500} < 0\,g\,kg^{-1}\,h^{-1}$, indicating drying in the midtroposphere by vertical advection (diamonds); 64 events with $VADV_{500}$ between 0 and $0.03\,g\,kg^{-1}\,h^{-1}$, indicating moderate moistening (crosses); and 136 events with $VADV_{500} > 0.03\,g\,kg^{-1}\,h^{-1}$, indicating strong moistening (triangles). It is evident from Fig. 9 that the mean frequency of the Cg cells (solid lines) is independent of $VADV_{500}$. In contrast, the mean frequency of the Cb cells increases strongly with increasing $VADV_{500}$. Notably, there are 75 events with at least 42 Cg cells per hour, but very few Cb cells occurring in the subsequent hours because the vertical advection term associated with these events is negative (drying). The second and third panels of Fig. 9 repeat the composite analysis of the mean Cg cell (solid) and Cb cell (dashed) frequencies around events for the DW and ME regimes, respectively. While there is some effect of the large-scale regime on the evolution of the cell modes, qualitatively the two regimes behave very similarly to each other and the overall behavior. Independent of synoptic regime it is the increased moistening in the midtroposphere by vertical advection and not with the existence of Cg cells that explains the difference in the number of Cb cells.

6. Summary

This study used C-band radar data in the Darwin region to identify two types of convective cloud cells with a 0-dBZ cloud-top height (CTH) between 3 and 7 km ($Cu_{3km–7km}$). These two modes are the congestus (Cg) clouds, which terminate their growth around the freezing level, and the cumulonimbus (Cb) clouds, which grow into deeper convection at a later time. This was achieved by examining the statistical properties of cell top heights in a sequence of radar scans. Based on this approach, we were able to classify 70% of the entire $Cu_{3km–7km}$ population (CTH < 7 km) during two wet seasons at Darwin as either Cg or Cb cells. Of the classified $Cu_{3km–7km}$ cells, 26% are found to be Cb cells that will ascend to greater altitude at a later time, while 74% of the $Cu_{3km–7km}$ cells were found to never grow deeper than 7 km. This Cb to Cg splitting ratio is found to be invariant of the five large-scale Darwin regimes. Note there is a third cumulus cloud type with tops between 3 and 7 km: the nonprecipitating cumulus cloud. However, this cloud type cannot be easily detected by the C-band radar and is estimated to be as much as one-third of cumulus populations with tops between 3 and 7 km.

The cells classified as Cb are observed to have larger radar reflectivities, rain rates, and drop size at the lowest radar level (2.5 km) compared to the Cg cells. If the

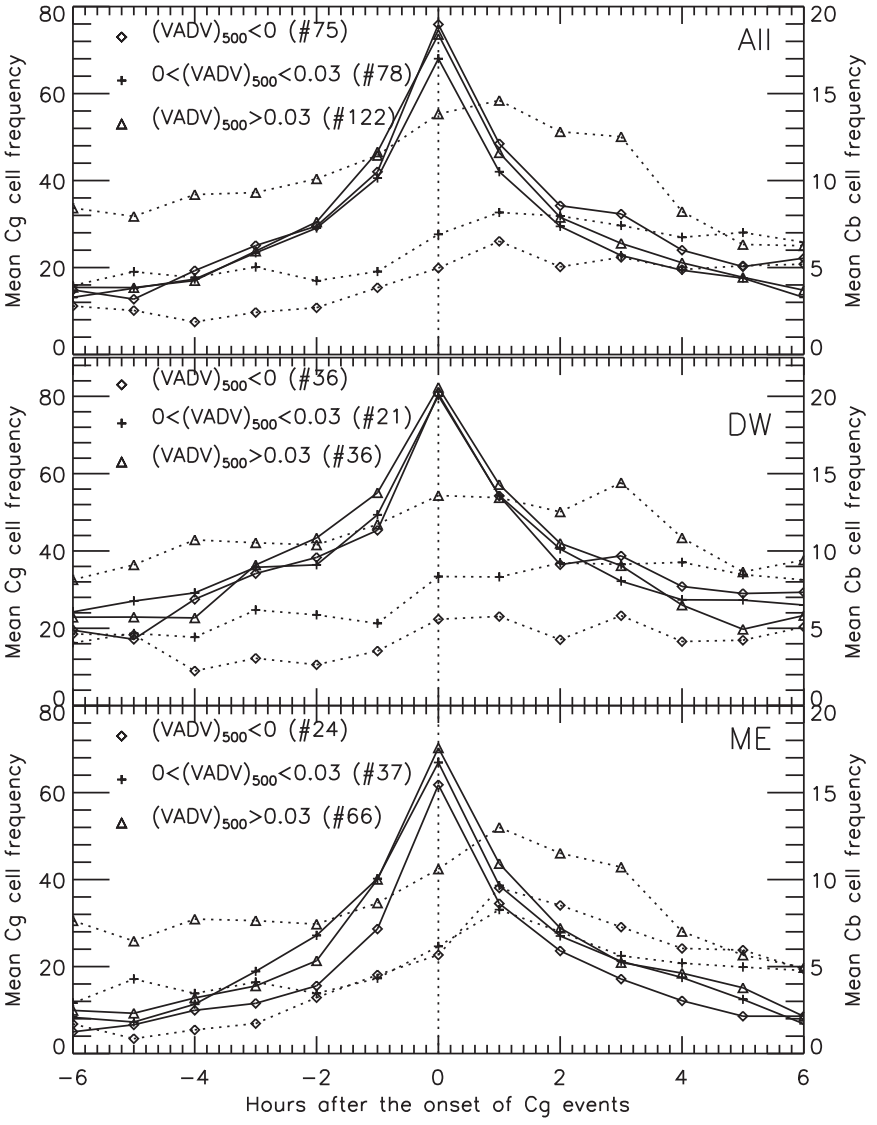

FIG. 9. Composite evolution of the Cg (solid lines) and Cb (dashed lines) cell occurrence frequency for 6 h on either side of the Cg cell peak occurrence events ($t = 0$). Mean cell occurrence frequencies in three different bins of the midtroposphere large-scale vertical advection of moisture ($VADV_{500}$): (top) all events, and events in the (middle) DW and (bottom) ME regime.

atmospheric conditions during both modes were similar, then it could be argued that it is the microphysical properties of Cb cells themselves that lead to stronger growth. However, the atmospheric conditions between the two $Cu_{3km–7km}$ modes were found to differ and are likely to play a significant role in determining which $Cu_{3km–7km}$ cell will be able to grow.

Combining the cell attributes from the radar analysis with radiosonde observations and results from the derived large-scale budget analyses in the Darwin region allowed the investigation of the relationship of the dynamic and thermodynamic state of the atmosphere with the two $Cu_{3km–7km}$ modes. In particular, we were able to investigate the conditions leading up to the occurrence of Cb cells, thereby shedding more light on the processes involved in the transition from shallow to deep convection. In the hours preceding the Cb cells, strong, well-defined enhancement in humidity occurs in the midtroposphere (5–10 km). In contrast, the midtroposphere is significantly drier prior to high occurrences of Cg cells. So, consistent with several previous studies, the moisture profiles of the midtroposphere have a strong impact on the vertical development of tropical cumulus clouds, and the presence of moisture in the midtroposphere

appears strongly related to the development of deep convective clouds. However, this study has shown that large numbers of $Cu_{3km-7km}$ cells exist prior to the development of both Cg and Cb cell populations, making it less likely that Cg moistening alone can explain the transition to deeper convection. Instead, it was shown that it is the presence of moistening by large-scale vertical advection, or simply the presence of large-scale upward motion, that is crucial to the development of Cb cells in relatively large proportions after the existence of the Cg cells. In contrast, when the large-scale motion is found to be downward very few Cb cells can form even though large numbers of Cg cells are present in the vicinity. While the overall number of Cb cells showed some dependence on the synoptic regime, the mechanisms for the transition from $Cu_{3km-7km}$ to deep convection were found to be independent of the large-scale regimes, lending additional confidence to the results. These results confirm the crucial importance of dynamical processes and their interplay with the convective cloud population in the transition from shallow to deep convection in the tropics.

Acknowledgments. This work has been supported by the U.S. Department of Energy ARM Grant DE-FG02-09ER64742. We would like to acknowledge the contributions of Brad Atkinson and Michael Whimpey in supporting the Darwin observatory and data management. V. Kumar thanks Rodney Potts, Joshua Soderholm, and Chris Chambers for their discussion on cell selection criteria.

REFERENCES

Arakawa, A., 2004: The cumulus parameterization problem: Past, present, and future. *J. Climate,* **17,** 2493–2525.

Bringi, V. N., C. R. Williams, M. Thurai, and P. T. May, 2009: Using dual-polarized radar and dual-frequency profiler for DSD characterization: A case study from Darwin, Australia. *J. Atmos. Oceanic Technol.,* **26,** 2107–2122.

Casey, S. P. F., E. J. Fetzer, and B. H. Kahn, 2012: Revised identification of tropical oceanic cumulus congestus as viewed by CloudSat. *Atmos. Chem. Phys.,* **12,** 1587–1595.

Chu, P. S., and J. Wang, 1997: Tropical cyclone occurrences in the vicinity of Hawaii: Are the differences between El Niño and non–El Niño years significant? *J. Climate,* **10,** 2683–2689.

Davies, L., C. Jakob, P. T. May, V. V. Kumar, and S. Xie, 2013: Relationships between the large-scale atmosphere and the small-scale state for Darwin, Australia. *J. Geophys. Res.,* **118,** 11 534–11 545, doi:10.1002/jgrd.50645.

Derbyshire, S. H., I. Beau, P. Bechtold, J.-Y. Grandpeix, J.-M. Piriou, J.-L. Redelsperger, and P. M. Soares, 2004: Sensitivity of moist convection to environmental humidity. *Quart. J. Roy. Meteor. Soc.,* **130,** 3055–3080.

Dixon, M., and G. Wiener, 1993: TITAN: Thunderstorm identification, tracking, analysis, and nowcasting—A radar-based methodology. *J. Atmos. Oceanic Technol.,* **10,** 785–797.

Hohenegger, C., and B. Stevens, 2013: Preconditioning deep convection with cumulus congestus. *J. Atmos. Sci.,* **70,** 448–464.

Holloway, C., and J. Neelin, 2009: Moisture vertical structure, column water vapor, and tropical deep convection. *J. Atmos. Sci.,* **66,** 1665–1683.

Jakob, C., 2010: Accelerating progress in global atmospheric model development through improved parameterizations: Challenges, opportunities, and strategies. *Bull. Amer. Meteor. Soc.,* **91,** 869–875.

Jensen, M. P., and A. D. Del Genio, 2006: Factors limiting convective cloud-top height at the ARM Nauru Island climate research facility. *J. Climate,* **19,** 2105–2117.

Johnson, R. H., T. M. Rickenbach, S. A. Rutledge, P. E. Ciesielski, and W. H. Schubert, 1999: Trimodal characteristics of tropical convection. *J. Climate,* **12,** 2397–2418.

Keenan, T. D., K. Glasson, F. Cummings, T. S. Bird, J. Keeler, and J. Lutz, 1998: The BMRC/NCAR C-band polarimetric (CPOL) radar system. *J. Atmos. Oceanic Technol.,* **15,** 871–886.

Kemball-Cook, S. R., and B. C. Weare, 2001: The onset of convection in the Madden–Julian oscillation. *J. Climate,* **14,** 780–793.

Kikuchi, K., and Y. N. Takayabu, 2004: The development of organized convection associated with the MJO during TOGA COARE IOP: Trimodal characteristics. *Geophys. Res. Lett.,* **31,** L10101, doi:10.1029/2004GL019601.

Kumar, V. V., C. Jakob, A. Protat, P. T. May, and L. Davies, 2013a: The four cumulus cloud modes and their progression during rainfall events: A C-band polarimetric radar perspective. *J. Geophys. Res.,* **118,** 8375–8389, doi:10.1002/jgrd.50640.

——, A. Protat, P. T. May, C. Jakob, G. Penide, S. Kumar, and L. Davies, 2013b: On the effects of large-scale environment and surface conditions on convective cloud characteristics over Darwin, Australia. *Mon. Wea. Rev.,* **141,** 1358–1374.

Lin, X., and R. H. Johnson, 1996: Heating, moistening, and rainfall over the western Pacific warm pool during TOGA COARE. *J. Atmos. Sci.,* **53,** 3367–3383.

Luo, Z., G. Y. Liu, G. L. Stephens, and R. H. Johnson, 2009: Terminal versus transient cumulus congestus: A CloudSat perspective. *Geophys. Res. Lett.,* **36,** L05808, doi:10.1029/2008GL036927.

Mapes, B. E., S. Tulich, J. Lin, and P. Zuidema, 2006: The mesoscale convection life cycle: Building block or prototype for large-scale tropical waves? *Dyn. Atmos. Oceans,* **42,** 3–29.

May, P. T., J. H. Mather, G. Vaughan, C. Jakob, G. M. McFarquhar, K. N. Bower, and G. G. Mace, 2008: The Tropical Warm Pool International Cloud Experiment. *Bull. Amer. Meteor. Soc.,* **89,** 629–645.

——, C. Long, and A. Protat, 2012: The diurnal cycle of the boundary layer, convection, clouds, and surface radiation in a coastal monsoon environment (Darwin Australia). *J. Climate,* **25,** 5309–5326.

Moran, K. P., B. E. Martner, M. J. Post, R. A. Kropfli, D. C. Welsh, and K. P. Widener, 1998: An unattended cloud-profiling radar for use in climate research. *Bull. Amer. Meteor. Soc.,* **79,** 443–455.

Nuijens, L., B. Stevens, and A. Siebesma, 2009: The environment of precipitating shallow cumulus convection. *J. Atmos. Sci.,* **66,** 1962–1979.

Penide, G., V. V. Kumar, A. Protat, and P. T. May, 2013: Statistics of drop size distribution parameters and rain rates for stratiform and convective precipitation during the North Australian wet season. *Mon. Wea. Rev.,* **141,** 3222–3237.

Pope, M., C. Jakob, and M. Reeder, 2009: Regimes of the north Australian wet season. *J. Climate,* **22,** 6699–6715.

Powell, S. W., and R. A. Houze Jr., 2013: The cloud population and onset of the Madden-Julian Oscillation over the Indian Ocean during DYNAMO-AMIE. *J. Geophys. Res.,* **118,** 11 979–11 995, doi:10.1002/2013JD020421.

Redelsperger, J.-L., D. B. Parsons, and F. Guichard, 2002: Recovery processes and factors limiting cloud-top height following the arrival of a dry intrusion observed during TOGA COARE. *J. Atmos. Sci.,* **59,** 2438–2457.

Sherwood, S. C., and R. Wahrlich, 1999: Observed evolution of tropical deep convective events and their environment. *Mon. Wea. Rev.,* **127,** 1777–1795.

Steiner, M., R. A. Houze Jr., and S. E. Yuter, 1995: Climatological characterization of three-dimensional storm structure from operational radar and rain gauge data. *J. Appl. Meteor.,* **34,** 1978–2007.

Takemi, T., O. Hirayama, and C. Liu, 2004: Factors responsible for the vertical development of tropical oceanic cumulus convection. *Geophys. Res. Lett.,* **31,** L11109, doi:10.1029/2004GL020225.

Tao, W.-K., D. Starr, A. Hou, P. Newman, and Y. Sud, 2003: A cumulus parameterization workshop. *Bull. Amer. Meteor. Soc.,* **84,** 1055–1062.

Testud, J., S. Oury, P. Amayenc, and R. A. Black, 2001: The concept of ''normalized'' distributions to describe raindrop spectra: A tool for cloud physics and cloud remote sensing. *J. Appl. Meteor.,* **40,** 1118–1140.

Xie, S., R. T. Cederwall, and M. Zhang, 2004: Developing long-term single-column model/cloud system–resolving model forcing data using numerical weather prediction products constrained by surface and top of the atmosphere observations. *J. Geophys. Res.,* **109,** D01104, doi:10.1029/2003JD004045.

Yanai, M., S. Esbensen, and J. Chu, 1973: Determination of bulk properties of tropical cloud clusters from large-scale heat and moisture budgets. *J. Atmos. Sci.,* **30,** 611–627.

Zhang, M., and J. Lin, 1997: Constrained variational analysis of sounding data based on column-integrated budgets of mass, heat, moisture, and momentum: Approach and application to ARM measurements. *J. Atmos. Sci.,* **54,** 1503–1524.

Zhang, Y., and S. A. Klein, 2010: Mechanisms affecting the transition from shallow to deep convection over land: Inferences from observations of the diurnal cycle collected at the ARM Southern Great Plains site. *J. Atmos. Sci.,* **67,** 2943–2959.

Zipser, E. J., and K. R. Lutz, 1994: The vertical profile of radar reflectivity of convective cells: A strong indicator of storm intensity and lightning probability? *Mon. Wea. Rev.,* **122,** 1751–1759.

Zrnić, D. S., and A. V. Ryzhkov, 1999: Polarimetry for weather surveillance radars. *Bull. Amer. Meteor. Soc.,* **80,** 389–406.